





## Predictability of Coastal Boundary Layer Jets in South China Using Atmosphere–Ocean Coupling

Jingwei Xu<sup>1,2,3</sup> , Xiefei Zhi<sup>1</sup> , Dmitry V. Sein<sup>4,5</sup>, William Cabos<sup>6</sup> , Yong Luo<sup>7</sup> , Ling Zhang<sup>1</sup>, Fu Dong<sup>1</sup>, Klaus Fraedrich<sup>2</sup>, and Daniela Jacob<sup>3</sup>

**Key Points:**

- The use of atmosphere–ocean coupling can improve the predictability of coastal boundary layer jets in South China
- The coupled model gave a more realistic sea surface temperature standard deviation and corrected the overestimated air temperature
- Strong air–sea mixing led to a more robust inertial oscillation, veering the ageostrophic flows toward the direction of the maximum wind

<sup>1</sup>Key Laboratory of Meteorological Disaster, Ministry of Education (KLME)/ Joint International Research Laboratory of Climate and Environment Change (ILCEC)/ Collaborative Innovation Center on Forecast and Evaluation of Meteorological Disasters (CIC-FEMD)/ Joint Center for Data Assimilation Research and Applications, Nanjing University of Information Science and Technology (NUIST), Nanjing, China, <sup>2</sup>Max Planck Institute for Meteorology, Hamburg 20146, Germany, <sup>3</sup>Climate Service Center Germany (GERICS)/ Helmholtz-Zentrum Hereon, Hamburg 20095, Germany, <sup>4</sup>Alfred Wegener Institute (AWI), Bremerhaven 27568, Germany, <sup>5</sup>Shirshov Institute of Oceanology, Russian Academy of Sciences, Moscow, Russia, <sup>6</sup>Universidad de Alcalá, Madrid, Spain, <sup>7</sup>Ministry of Education Key Laboratory for Earth System Modeling, Department of Earth System Science, Tsinghua University, Beijing, China

**Correspondence to:**

J. Xu,  
xu\_jw@sina.cn

**Citation:**

Xu, J., Zhi, X., Sein, D. V., Cabos, W., Luo, Y., Zhang, L., et al. (2023). Predictability of coastal boundary layer jets in South China using atmosphere–ocean coupling. *Journal of Geophysical Research: Atmospheres*, 128, e2023JD039184. <https://doi.org/10.1029/2023JD039184>

Received 3 MAY 2023  
Accepted 29 JUL 2023

**Author Contributions:**

**Conceptualization:** Jingwei Xu, Xiefei Zhi  
**Investigation:** Jingwei Xu  
**Methodology:** Jingwei Xu  
**Project Administration:** Xiefei Zhi  
**Resources:** Dmitry V. Sein, William Cabos  
**Software:** Ling Zhang, Fu Dong  
**Supervision:** Xiefei Zhi, Yong Luo, Klaus Fraedrich, Daniela Jacob  
**Validation:** Jingwei Xu  
**Writing – original draft:** Jingwei Xu  
**Writing – review & editing:** Dmitry V. Sein, William Cabos

**Abstract** Most standalone atmospheric models do not perform well in simulations of coastal boundary layer jets (BLJs), important weather processes that can trigger heavy rain in coastal areas by supplying both moisture and dynamic lifting. We compared 33-year simulations with a coupled atmosphere–ocean model and its standalone atmospheric component, the REgional atmosphere Model (REMO), forced by the prescribed sea surface temperature (SST). We validated our results using the Tropical Rainfall Measuring Mission SST and the ERA5 hourly reanalysis data set. We found that the coupled model gave a more realistic SST standard deviation than the REMO on BLJ days and corrected the overestimated air temperature over land during the day. The coupled atmosphere–ocean model showed a lower land–sea thermal contrast in the boundary layer. This increased the effects of inertial oscillation, which caused the ageostrophic flows to veer southwest, which is the direction of the maximum wind speed on BLJ days. This reproduced a more reasonable land–sea thermal contrast in the boundary layer as a result of strong air–sea mixing in coastal weather processes, which led to a more robust inertial oscillation and a larger SST standard deviation over the central South China Sea. These findings deepen our understanding of the influence of a fully mixed air–sea boundary on coastal weather processes. These results show that operational numerical weather prediction models can be improved by applying atmosphere–ocean coupling to advance their ability to forecast the weather (e.g., BLJ events) in coastal areas.

**Plain Language Summary** Coastal boundary layer jets (BLJs) are important coastal weather processes and, because they are precursor signals of heavy rain, they can be used to improve operational numerical weather forecasts. Coupled atmosphere–ocean models improve the predictability of BLJs in South China, but we still need a deeper understanding of the mechanism leading to their occurrence. We compared 33-year simulations with a coupled atmosphere–ocean model and its standalone atmospheric component forced by the prescribed sea surface temperature (SST). Through validation against remote sensing SSTs and ERA5 hourly reanalysis data, we found that the coupled model gave a more realistic SST standard deviation and corrected the overestimated air temperature over land surfaces. These improvements helped the coupled atmosphere–ocean model to reproduce a more reasonable land–sea thermal contrast in the boundary layer as a result of strong air–sea mixing in coastal weather processes, which led to a more robust inertial oscillation and a larger SST standard deviation over the central South China Sea. We conclude that the impact of the influence of a fully mixed air–sea boundary on coastal weather processes is larger than previously recognized.

### 1. Introduction

Boundary layer jets (BLJs) occur below a height of 1 km (900 hPa) and usually trigger heavy rainfall by supplying both moisture and dynamic lifting (Du & Chen, 2019). The BLJs over coastal areas are not only caused by a large-scale land–sea thermal contrast, inertial oscillation and the terrain, but also by large-scale atmospheric systems (Kong et al., 2020)—for example, the subtropical high. The heavy rain that usually accompanies BLJs in coastal areas (Du & Chen, 2019) can result in significant economic losses because our ability to forecast heavy

© 2023. The Authors.

This is an open access article under the terms of the [Creative Commons Attribution License](https://creativecommons.org/licenses/by/4.0/), which permits use, distribution and reproduction in any medium, provided the original work is properly cited.

rain is low in these regions (Du et al., 2022; Zhang & Meng, 2019) and because stronger economies are largely located in coastal cities. An example is the warm sector heavy rainfall that occurs in southern China during the early summer rainy season (Du et al., 2022).

Rainfall in South China shows a diurnal variation (Wu et al., 2020). In many regions—for example, over the coastal area of Guangdong—rainfall initially occurs in the morning and then propagates inland in the afternoon (Chen et al., 2018). The onset of this rainfall occurs over coastal areas, but the precursor signals occur over the sea. The precise prediction of these precursors would greatly improve operational weather forecasts (Dong et al., 2021). However, standalone atmospheric models have a limited ability to forecast BLJs as a result of the complexity of air–sea interactions in coastal weather processes. We therefore need to apply a coupled atmosphere–ocean model to gain a deeper understanding of the mechanism linking air–sea interactions and the occurrence of BLJs before we can improve operational numerical weather forecasts.

The traditional view is that air–sea interactions should only be taken into consideration in extended-range ensemble weather forecasting (Chen et al., 2003). In most previous operational numerical weather prediction models, medium-range forecasts only use standalone atmospheric models and the prescribed sea surface temperature (SST) (e.g., the Global Forecast System from the National Centers for Environmental Prediction and the Global/Regional Assimilation Prediction System from the China Meteorological Administration). Since June 2018, all operational configurations of the European Centre for Medium-range Weather Forecasts (ECMWF) Integrated Forecasting System have been coupled to an ocean model (Browne et al., 2019), which has dramatically improved the forecasting of typhoons. However, the reason why the use of a coupled atmosphere–ocean model improves our ability to forecast coastal weather events is still unclear. We therefore validated a coupled atmosphere–ocean model and analyzed the main mechanism behind the triggering of BLJs using a fully coupled model. We conclude that the impact of the influence of a fully mixed air–sea boundary on coastal weather processes is larger than previously recognized.

The structure of this paper is as follows. Section 2 describes the data, model, experimental setup and method for identifying BLJs. Section 3 presents the validation of the simulated SST with Tropical Rainfall Measuring Mission (TRMM) data and the simulated BLJ processes are compared with the ERA5 reanalysis data set (Hersbach et al., 2020). We then investigate why many BLJs cannot be simulated by a standalone atmospheric model is discussed, with particular emphasis on the relation between the large-scale land–sea thermal contrast and inertial oscillation. Our main conclusions and discussion are presented in Section 4.

## 2. Data and Methodology

### 2.1. Model Components and Experimental Setup

We used a regionally coupled ocean–atmosphere model (Sein et al., 2015) consisting of the REgional Atmosphere MOdel (REMO) (e.g., Jacob, 2001; Jacob et al., 2001), the Max Planck Institute Ocean Model (MPIOM) and the Hydrological Discharge (HD) model (Hagemann & Dümenil, 1997; Hagemann & Gates, 2001), which are coupled via the Ocean Atmosphere Sea Ice Soil Version 3 (OASIS3) model (Valcke et al., 2010, 2015). We use the acronym ROM (REMO-OASIS-MPIOM) for the REMO/MPIOM/HD coupled model. All the components of the ROM are run in a global configuration, except for REMO. We applied the ROM to reproduce the climatology of the East Asian summer monsoon system. In parallel, we also used the standalone atmospheric model REMO to investigate the impacts of regional atmosphere–ocean coupling.

The SST and other sea surface conditions in the ROM are passed from the MPIOM to the REMO at intervals of 3 hr. In the standalone REMO, the SST is prescribed from the reanalysis SST every 6 hr and linearly interpolated for every REMO time step. Figure 1a shows the REMO domain and the MPIOM computational grid. The main difference between the REMO and ROM experiments is that the REMO is forced by the reanalysis SST, whereas the ROM is forced by the full air–sea mixed boundary. Previous studies have shown that the ROM can present a stronger mixed air–sea boundary than the REMO (Sein et al., 2017; Xu et al., 2019; Zhu et al., 2020).

The ocean model MPIOM was developed at the Max Planck Institute for Meteorology (Jungclaus et al., 2013; Marsland et al., 2003). The MPIOM is a free surface, primitive equations ocean model formulated on an orthogonal curvilinear Arakawa C-grid (Arakawa & Lamb, 1977). The MPIOM curvilinear grid has shifted poles located over the land surface to avoid the numerical singularity associated with the convergence of meridians. This means

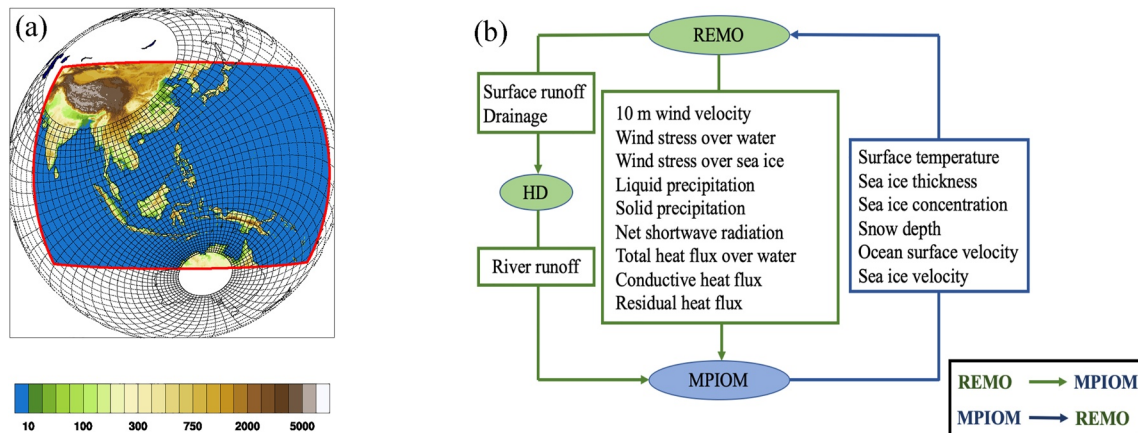


**Figure 1.** (a) Model grid configuration as described by Sein et al. (2015). The red rectangle denotes the coupled area (the REMO domain and orography; units: m) and the black lines represent the Max Planck Institute Ocean Model (MPIOM) grid (every 12th grid line is shown). (b) Model coupling scheme in the coupled area. The data flow from the REMO to the MPIOM is marked by green arrows and the data flow from the MPIOM to the REMO is marked by the blue arrow.

that the model can reach a high resolution regionally and maintain a global domain. To ensure model stability, 40 vertical layers were set from 10 to 500 m in the deep ocean. It is spun-up twice for 45 years (1958–2002) with forcing by the ERA-40 reanalysis data set. After ocean spin-up in the standalone mode, the model is coupled with the REMO regional climate model using the ERA-40 reanalysis data set as the lateral boundary conditions for 45 years (1958–2002). The restart files obtained from the simulation for 31 December 2002 were used as the initial conditions for the ROM spin-up with forcing by the ERA Interim data set (an additional 21 years for 1980–2000). The model state obtained for 31 December 2000 (after 156 years of spin-up for the ocean and 66 years for the REMO) was used as the initial conditions in our simulations.

The REMO atmospheric model has a horizontal resolution of 25 km and 27 hybrid vertical layers. The domain mainly covers the western North Pacific and the main CORDEX East Asia domain (Figure 1a). A rotated grid is applied in the REMO configuration to avoid the very different extensions of grid cells close to the poles. The dynamic core of the model and the discretization in space and time are based on the Europa Model of the German Weather Service (Majewski, 1991). The physical parameterizations are taken from the GCM ECHAM versions 4 and 5 (Roeckner et al., 1996, 2003). The prognostic variables of the REMO are the surface pressure, the horizontal wind components, the temperature, the water vapor content, the liquid water content and cloud ice. The horizontal discretization is performed on the Arakawa C-grid and the hybrid vertical coordinates are defined according to Simmons and Burridge (1981). The time discretization is based on the leap frog scheme with semi-implicit correction and Asselin filter smoothing (Asselin, 1972). The SST and sea ice distribution are prescribed as the lower boundary values for the ocean grid points. In the uncoupled simulations, they are taken from the ERA Interim reanalysis data set, whereas they are taken from the MPIOM model in the coupled model. The initial conditions for the REMO model are the state obtained from the 66-year ROM spin-up. The lateral boundary forcing is obtained from the ERA Interim reanalysis data set for both the standalone and coupled models.

The terrestrial HD model (Hagemann & Dumenil, 1998; Hagemann & Gates, 2001) is run over the whole globe topography with constant a  $0.5^\circ$  resolution to simulate the lateral fluxes of freshwater at the land surface with a daily time step. The sum of the three flow processes consists of the total outflow of a grid box (i.e., the lateral water flow), which includes overland flow, base flow and river flow. More information can be found in the model description (Hagemann & Gates, 2001).

The OASIS3 coupler was developed by the European Centre for Research and Advanced Training in Scientific Computation (CERFACS). In the areas coupled via OASIS3, the ocean model receives heat, freshwater and momentum fluxes from the REMO with an interval of 3 hr and passes the sea surface conditions to the REMO (Figure 1b). In the uncoupled area, the ocean model MPIOM calculates heat, freshwater and momentum fluxes from the reanalysis data set, which simultaneously drives the REMO. Detailed model coupling descriptions have been documented by Sein et al. (2015).

## 2.2. Identification of BLJ

As suggested by Du and Rotunno (2014) and Tu et al. (2019), we identified the BLJs on the basis of the following criteria: (a) a maximum wind speed  $>10 \text{ m s}^{-1}$  below 900 hPa; (b) meridional winds  $>0$  ( $v > 0 \text{ m s}^{-1}$ ); and (c) below 600 hPa, the wind speed must decrease by at least  $3 \text{ m s}^{-1}$  from the height of the maximum wind speed in the boundary layer to the minimum wind speed above the boundary layer.

## 2.3. Elimination of the Influence of Tropical Cyclones

The climate of South China is also influenced by tropical cyclones. Unlike previous studies, we eliminated the influence of tropical cyclones on the BLJ grid points in our study area by excluding the BLJ grid points on which a tropical cyclone was active in the region. We followed the method of Sinclair (2004) to identify tropical cyclones in the ROM and REMO simulation results and defined the area of influence of a tropical cyclone as the region within 500 km from its center (Luo et al., 2016; Ren et al., 2006, 2007).

A low-pressure center must meet the following four criteria: (a) have a maximum of 850 hPa relative vorticity greater than  $+2.5 \times 10^{-5} \text{ s}^{-1}$  within a radius of 150 km; (b) have a maximum 250–850 hPa thickness  $>935 \text{ dam}$  within a radius of 150 km (indicating a deep warm core structure); (c) generate a surface (10 m) wind speed  $>11.3 \text{ m s}^{-1}$  within a radius of 225 km; and (d) evolve in a barotropic or weakly baroclinic environment, defined here by  $B < 25 \text{ m}$ . We used Equation 1 to calculate  $B$ :

$$B = \overline{(Z_{600} - Z_{925})_{\text{warm}}} - \overline{(Z_{600} - Z_{925})_{\text{cold}}} \quad (1)$$

where  $Z_{600}$  and  $Z_{925}$  are the 600 and 925 hPa heights and the overbars indicate the areal means over the semi-circles on the warm and cold sides of the average thermal wind vector. The BLJ grid points were eliminated over the area of influence of the tropical cyclone, defined as the region within a circle of 500 km radius from the center of the tropical cyclone (Luo et al., 2016; Ren et al., 2006, 2007). We used the historical best-track tropical cyclone data from the China Meteorological Administration (Lu et al., 2021) to remove the influence of tropical cyclones from the ERA5 BLJ events.

## 2.4. ERA5 Hourly Reanalysis Data Set

We used the latest atmospheric reanalysis data set (ERA5) from the ECMWF to test the BLJ results and related atmospheric process simulated by the REMO and ROM. This data set has a  $(0.25^\circ \times 0.25^\circ)$  grid resolution at 1-hr intervals and 50 hPa intervals in the vertical direction. This data set has been widely used to identify BLJs (Dong et al., 2021; Du & Chen, 2019; Kalverla et al., 2019).

## 2.5. SSTs From the TRMM Microwave Imager

To validate the SST simulated by the ROM and REMO, we applied the SST retrievals from the TRMM microwave imager (TMI) swath SST with a resolution of  $(0.25^\circ \times 0.25^\circ)$ . The TMI SSTs were calculated using a retrieval algorithm based on radiative transfer, which precisely accounts for the effects of the SST and winds on surface emissivity as well as the effects of the atmosphere on the brightness temperature (Wentz et al., 2000). The microwave SSTs had a mean bias of  $-0.07^\circ\text{C}$  and a standard deviation of  $0.57^\circ\text{C}$  compared with the observations from the TAO/TRITON and PIRATA SSTs (Gentemann et al., 2004). The equatorial orbit of the TRMM over the South China Sea (SCS) allows the diurnal variability to be determined (Wu, 2010). We used matched years from the available TRMM SSTs and the ROM and REMO simulations from 1998 to 2012 to validate the SSTs.

## 3. Results

### 3.1. Main Characteristics of the BLJ From the REMO, ROM, and ERA5 Simulations

The BLJ primarily occurs over the northern SCS during the early summer rainy season in May and June (Dong et al., 2021) and only a few tropical cyclones reach the study area during this time period. We therefore focused on the BLJ in these months and eliminated the days influenced by tropical cyclones (see Section 2.3). There were two regions with a high frequency of BLJs over the northern SCS (with Hainan Island as a boundary; Figures 2a–2c).



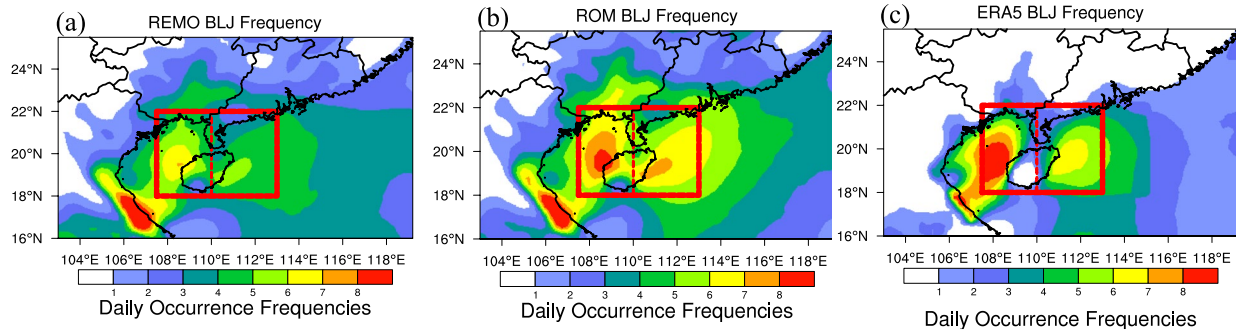


**Figure 2.** Daily mean occurrence of the boundary layer jet at 925 hPa in May and June during the time period 1980–2012 from the (a) REMO, (b) ROM, and (c) ERA5 data set, where the western box indicates the BLJ-West area and the eastern box indicates the BLJ-East area.

We defined the BLJ over the Beibu Gulf (Figure 2, western box) as the BLJ-West area and the BLJ off the coast of Guangdong (Figure 2, eastern box) as the BLJ-East area. In terms of the daily mean BLJ occurrence frequency, the ROM results were close to the ERA5 data set in the BLJ-West area, but slightly overestimated the occurrence of the BLJ in the BLJ-East area. The REMO clearly underestimated the occurrence frequency of the BLJ in both in the BLJ-West and the BLJ-East areas. The standalone atmospheric model (REMO) therefore seems to have a limited ability to reproduce the BLJ.

BLJ events were studied to determine the triggers for the BLJ. The hours in which >60% of the grid points in the western red box (eastern red box) reached the BLJ threshold were defined as BLJ-West (BLJ-East) events. To study the influence of diurnal variations, a BLJ-West (BLJ-East) day was defined as a day on which at least three BLJ-West (BLJ-East) events occurred (Dong et al., 2021; Du et al., 2022). If BLJ-West and BLJ-East events occurred on the same day, then this was defined as a double BLJ day and the other days were defined as pure BLJ-West (pure BLJ-East) days.

There were more BLJ days in June than in May—for example, there were 438 BLJ days in June and 259 BLJ days in May in the 33 years of the ERA5 data set. Double BLJ days constituted the major part of the BLJ-West and BLJ-East days in the ERA5 data set (52% of BLJ days), the ROM (67% of BLJ days) and the REMO (61% of BLJ days). There were more BLJ-West days than BLJ-East days in both May and June—for example, there were 218 BLJ-West days and 173 BLJ-East days in May and 404 BLJ-West days and 262 BLJ-East days in June in the ERA5 data set. The ROM simulated more BLJ days (945 days) than the REMO (750 days) and the ERA5 data set (687 days). The REMO underestimated the number of BLJ-West days in June, giving only 84% of the number in the ERA data set.

### 3.2. Validation of the SST Simulated by the ROM and REMO

The main difference between the REMO and ROM experiments is that the REMO is forced by the prescribed reanalysis SST, whereas the ROM is forced by a strong mixed air–sea boundary. Validation of the SST results can uncover the ability of the REMO and ROM to reproduce the SST. The diurnal variation of the SST has a key role in the land–sea thermal contrast (Dong et al., 2021; Du et al., 2015) and the land–sea thermal contrast and the inertial oscillation are also linked with the SST.

We used the TRMM TMI SSTs to validate the diurnal variability of the simulated SSTs in terms of the spatial distribution, standard deviation and variance of the monthly mean SST on BLJ days. We present the validation results in terms of the double BLJ days over the SCS (Figure 3) because double BLJ days are the main component of BLJ days. Similar validation results were obtained for BLJ-West and BLJ-East days (not shown). The double BLJ dates for TRMM are the double BLJ dates from ERA5 data set.

Figure 3 shows the distribution of the average SSTs on double BLJ days in the time period 1998–2012 and illustrates a clear SST gradient in the SCS. The SSTs were lower in the waters offshore the coast of Guangdong and were higher offshore the western Philippines. The SST bias in the ROM and REMO underestimated the SST in the waters offshore South China, but overestimated the SST offshore the southern Indochina Peninsula. There was a bias in the REMO SST despite the fact that the REMO uses the SST prescribed every 6 hr from the

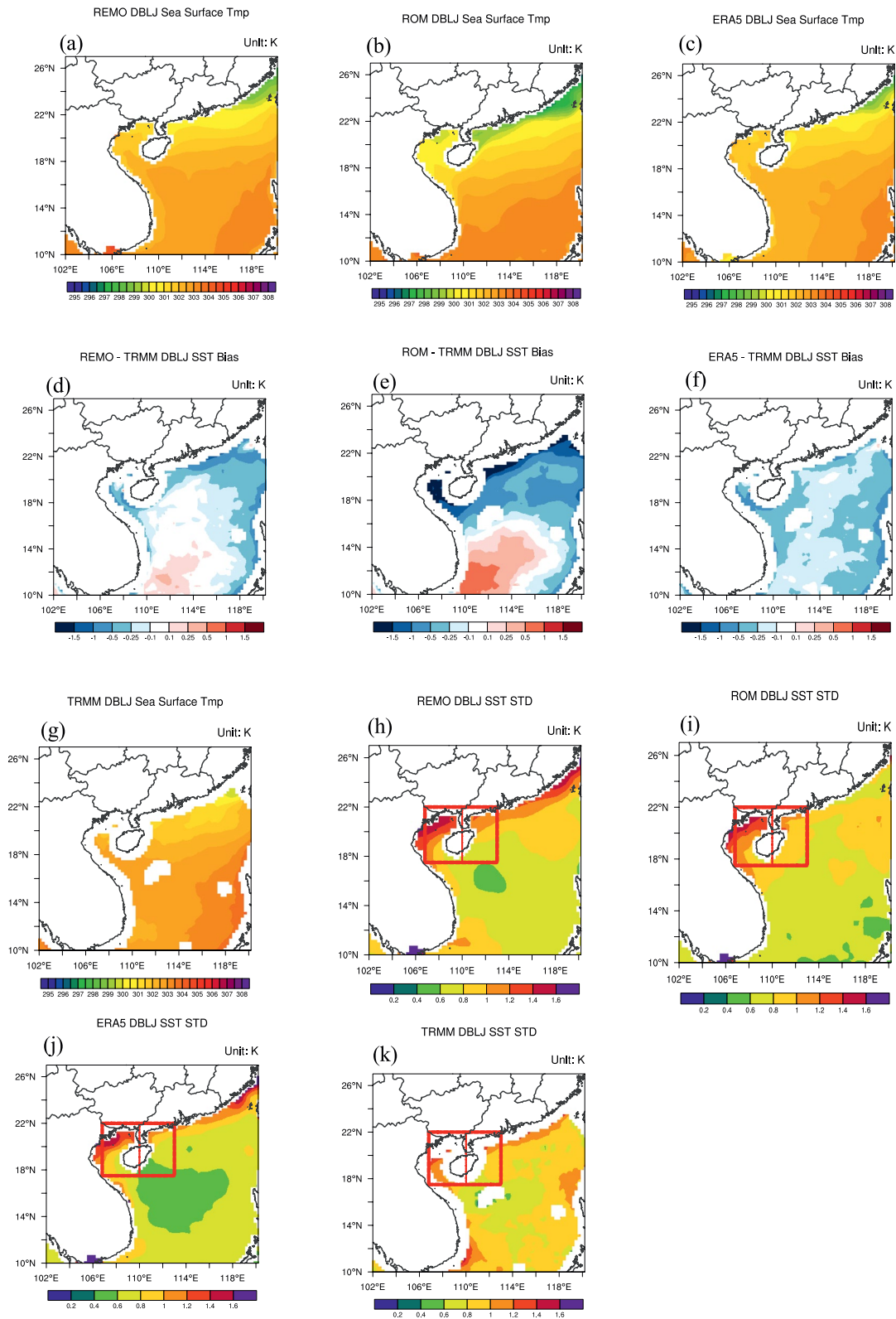
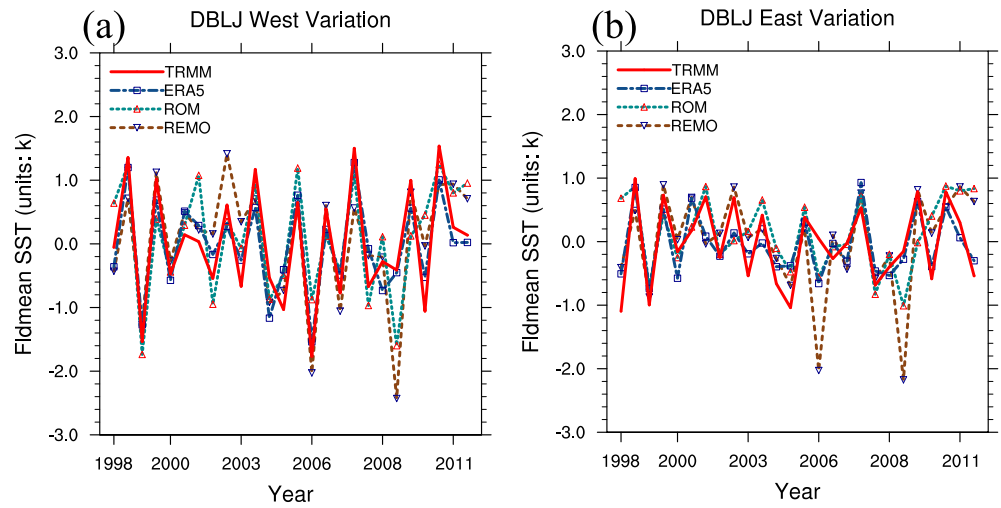


Figure 3.



**Figure 4.** Detrended monthly field-mean sea surface temperature (SST) variance against time from the (a) western and (b) eastern box. In the western box, the time correlation coefficient for the Tropical Rainfall Measuring Mission (TRMM) SST and the SSTs from the REMO, ROM and ERA5 data set were 0.76, 0.76, and 0.91, respectively. In the eastern box, the time correlation coefficient for the TRMM SST and the SSTs from the REMO, ROM and ERA5 data set were 0.51, 0.51, and 0.80, respectively.

reanalysis data set and linearly interpolates every time step (Figure 3d). The SST gradient in the ROM was greater than that in the REMO (Figure 3e). By contrast, the ERA5 SST showed a consistent slightly cold bias over the SCS (Figure 3f).

We validated the standard deviation of the hourly SSTs on double BLJ days to determine the magnitude of the diurnal variation of the SSTs. The standard deviations of the SSTs over the Beibu Gulf and the waters offshore Guangdong were higher than the standard deviation of the SST over the central SCS (Figures 3h–3k). Only the standard deviation from the ROM was as high as the standard deviation from the TRMM over the BLJ-West and BLJ-East areas (the western and eastern boxes in Figure 2). The magnitude of the SST variance from the ROM was more consistent with the actual SST variance over the area about 400 km off the Beibu Gulf coastline than all the other SSTs, including the prescribed reanalysis SST used by the REMO.

The variance of the detrended monthly mean SSTs on double BLJ days during the time period 1998–2012 showed that the SSTs from the REMO, ROM and the ERA5 data set were closely related to the TRMM data over the BLJ-West and BLJ-East areas (Figures 4a and 4b). The correlation coefficient from the BLJ-West area was much higher than that from the BLJ-East area. The time correlation coefficient of the REMO and ROM showed a similar correlation relationship, which means that the SSTs from both the REMO and ROM have a similar ability to represent the real monthly SST variance.

The REMO and ROM can therefore represent the spatial distribution and variance of the SST over the SCS on double BLJ days. The magnitude of the SST variance from the ROM was closer to the real conditions than the SST variance from the REMO. In addition, the SST from the ROM showed a stronger SST gradient over the SCS than the SST from the REMO. The higher standard deviation of the SST over the central SCS in the ROM indicated a greater SST response to the fully mixed air–sea boundary in the coupled model than that from the REMO.

### 3.3. Main Differences in the Field-Mean Wind Speed Between the ROM and REMO

If we consider the probability distribution of wind speeds  $>5.5 \text{ m s}^{-1}$ , then the ROM simulated more high wind speeds than the REMO, especially wind speeds  $>10 \text{ m s}^{-1}$  on both BLJ-West and BLJ-East days, whereas the

**Figure 3.** Average sea surface temperature (SST) on double boundary layer jet (BLJ) days in May and June during the time period 1998–2012 from the (a) REMO, (b) ROM and (c) ERA5 data set. The bias (d) between the REMO results and the Tropical Rainfall Measuring Mission (TRMM) data, (e) between the ROM results and the TRMM data, (f) between the ERA5 data set and the TRMM data. (g) The average SST on double BLJ days from the TRMM data. Standard deviation of the SSTs on double BLJ days in May and June during the time period 1998–2012 from the (h) REMO, (i) ROM, (j) ERA5 data set and (k) TRMM data. The white color over the South China Sea in indicates values that are missing from the TRMM (g, k). The western and eastern boxes were selected to analyze the variance of the SSTs against time.

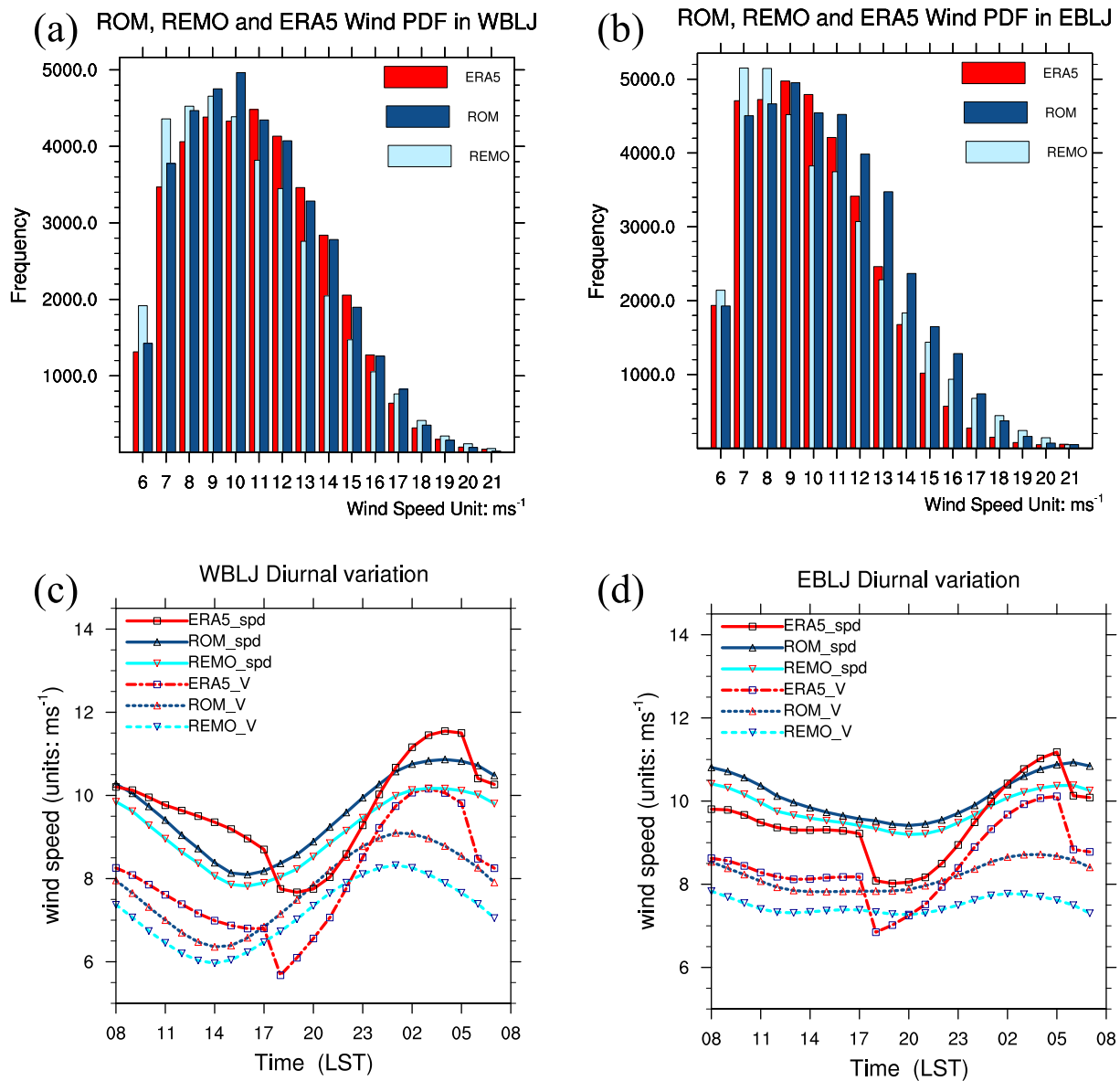


**Figure 5.** Frequency of occurrence of the field-mean wind speed in the range 5.5–21.5 m s<sup>-1</sup> in (a) the BLJ-West area and (b) the BLJ-East area. Diurnal variations in the wind speed and the meridional winds on (c) BLJ-West days and (d) BLJ-East days.

REMO showed a greater frequency of wind speeds <9 m s<sup>-1</sup> than the ROM (Figures 5a and 5b). The probability distribution of winds in the ROM was consistent with the ERA5 results for all wind speeds in the BLJ-West area and wind speeds of about 10 m s<sup>-1</sup> in the BLJ-East area; however, the frequency of wind speeds >12 m s<sup>-1</sup> was overestimated in the BLJ-East area.

We compared the diurnal variation in wind speeds and the meridional wind component on BLJ days and found that the REMO and ROM had a similar mean diurnal cycle (Figures 5c and 5d, light and dark blue lines). On BLJ-West days, the meridional wind speed was lowest at about 1400 Local Standard Time (LST), whereas the total wind speed was lowest at about 1600 LST on that day. Similar behavior was seen on BLJ-East days, with the lowest meridional and total wind speeds occurring at about 2000 LST. The diurnal variance of the wind speed in the ERA5 data set showed similar behavior (Figures 5c and 5d, red lines). The mechanism of the diurnal variance in the BLJ-West area was different from that in the BLJ-East area. The ageostrophic flow in the BLJ-West area is caused by large-scale land–sea breezes in the afternoon. By contrast, the ageostrophic flow in the BLJ-East area is triggered by planetary-scale land–sea breezes between the coastline of East Asia and about 145°E at night (Dong et al., 2021; Huang et al., 2010).



### 3.4. Differences in the Daily Mean Wind Field on BLJ Days

Figures 6a–6e shows the daily mean wind vectors at 925 hPa and the surface temperature and bias on BLJ days from the REMO and ROM compared with the ERA5 data set. All three sets of results show a similar daily mean wind distribution, with prevailing southwesterly winds on BLJ-West days (Figures 6a–6c). A comparison of the daily mean wind field from the ERA5 data set, the REMO and the ROM shows the main character of the daily mean airflow on BLJ-West days (Figures 6d and 6e). The ROM showed a stronger southwesterly wind speed than that in the REMO on BLJ-West days (Figure 6f). Similar biases and differences, but with greater magnitudes, were seen on BLJ-East days (Figures 6g–6i). The BLJ-East events are influenced by planetary-scale land–sea breezes between the coastline of East Asia and about 145°E (Dai & Deser, 1999; Dong et al., 2021; Huang et al., 2010) and there are more factors, such as tides (Dai & Wang, 1999) and thermal forcing (Huang et al., 2010), that can lead to differences in the winds on BLJ-East days.

The ROM perceptibly corrects the overestimated land surface temperature on both BLJ-West and BLJ-East days in this region, which means that the atmosphere transmits more energy to the ocean through a fully mixed air–sea boundary in this model than in the atmosphere-only REMO.

### 3.5. Mechanism to Improve the Predictability of the BLJ in the ROM

The large-scale land–sea breeze in the BLJ-West area and the planetary-scale land–sea breeze in the BLJ-East area are triggers of the ageostrophic flow (Dong et al., 2021). The wind deviations, defined as differences between the hourly wind field and the daily mean wind field, are derived from the large-scale land–sea thermal contrast and inertial oscillation and control when and where BLJ events occur. The inertial oscillation can cause the wind deviations to veer with a clear diurnal clockwise rotation. However, the significant inertial oscillation mostly occurs with the suppression of turbulence in the mixed layer, especially after sunset when the air–sea thermal contrast is lower (Blackadar, 1957). This means that the large-scale land–sea thermal contrast and the inertial oscillation have a see-saw relationship.

We present the results for double BLJ days because these constitute the majority of BLJ days. The wind deviations changes with air temperature were clearer on double BLJ days than on BLJ-West and BLJ-East days. The diurnal variance of the wind deviations from the ERA5 data set showed a clear link with the large-scale land–sea thermal contrast (Figures 7a, 7d, 7f, and 7g), especially at about 1700 LST (Figure 7f). After sunset, the north-easterly ageostrophic flow over the Beibu Gulf veered clockwise (Figure 7i, black line) as a result of the inertial oscillation. The wind speed was at a maximum when the direction of the wind deviations at about 0500 LST matched the daily mean value on that day. The results were similar for the BLJ-East area. However, only the planetary-scale land–sea breeze triggered the easterly ageostrophic flow off the Guangdong coastline between 2000 and 2300 LST. This planetary-scale land–sea breeze occurred later than the local-scale land–sea breeze (e.g., Du & Chen, 2019).

On double BLJ days, both the ROM and REMO showed a northeasterly ageostrophic flow over the Beibu Gulf in the afternoon, an easterly ageostrophic flow off the coastline of Guangdong at night and the inertial oscillation. These are all key features in the diurnal variance of the wind deviations. The air temperature over the northern Indochina Peninsula was much higher in the ROM and REMO than in the ERA5 data set, which weakened the inertial oscillation effect and led to a smaller variance of the wind speed during the night. The easterly ageostrophic flow off the coastline at night (Figures 8a–8c) and the ageostrophic flow over the Beibu Gulf in the afternoon (Figures 8f and 8g) were both lower in the ROM than in the ERA5 data set and the REMO. This means that the large-scale land–sea thermal contrast in the afternoon and at night were both lower in the ROM than in the ERA5 data set and the REMO.

The large-scale land–sea thermal contrast and the inertial oscillation showed a see-saw relationship. The smaller large-scale land–sea thermal contrast in the ROM indicated that the inertial oscillation effect was more robust than in the REMO. This was shown by a clear clockwise rotation in the difference in the diurnal variance of the wind deviations between the ROM and the REMO (Figure 8i). The large-scale land–sea thermal contrast caused by warming during the day and cooling at night was lower in the ROM than in the REMO, especially in the afternoon and at night (Figures 8b–8d, 8f, and 8g).

We plotted two composite vertical cross-sections including the BLJ-West and BLJ-East areas to investigate why the large-scale land–sea thermal contrast was lower in the ROM than in the REMO. The daily mean vertical

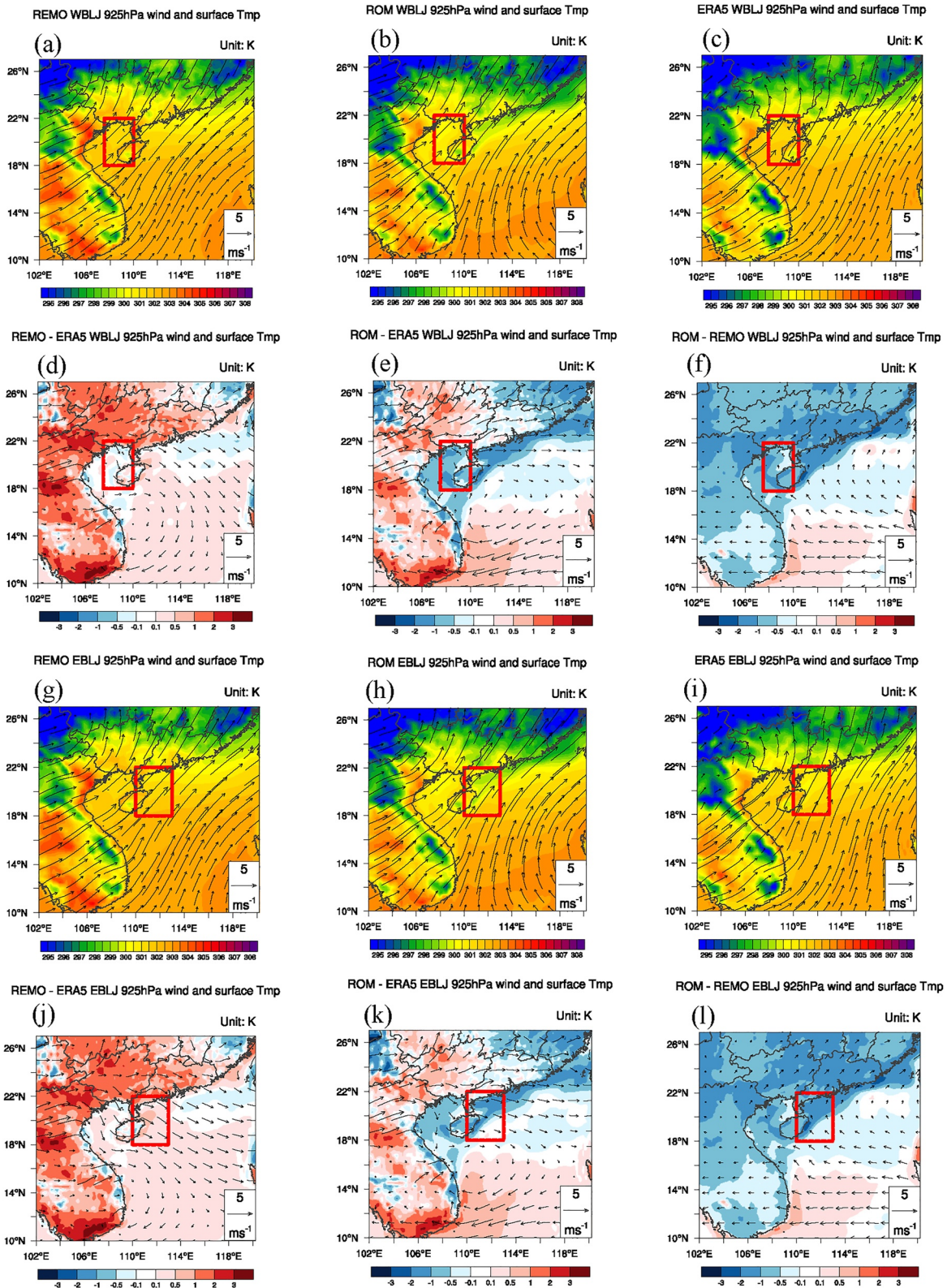


**Figure 6.** Daily mean wind field at 925 hPa and the surface temperature on BLJ-West days in the (a) REMO, (b) ROM, (c) ERA5 data set, (d) bias ROM-ERA5, (e) bias ROM-ERA5, (f) the differences between the ROM and REMO. Daily mean wind field at 925 hPa and the surface temperature on BLJ-East days in the (g) REMO, (h) ROM, (i) ERA5 data set, (j) bias ROM-ERA5 and (k) bias ROM-ERA5. (l) The differences between the ROM and REMO. The colors represent the surface temperature and the vectors indicate the wind; the red box outlines the BLJ-East area.



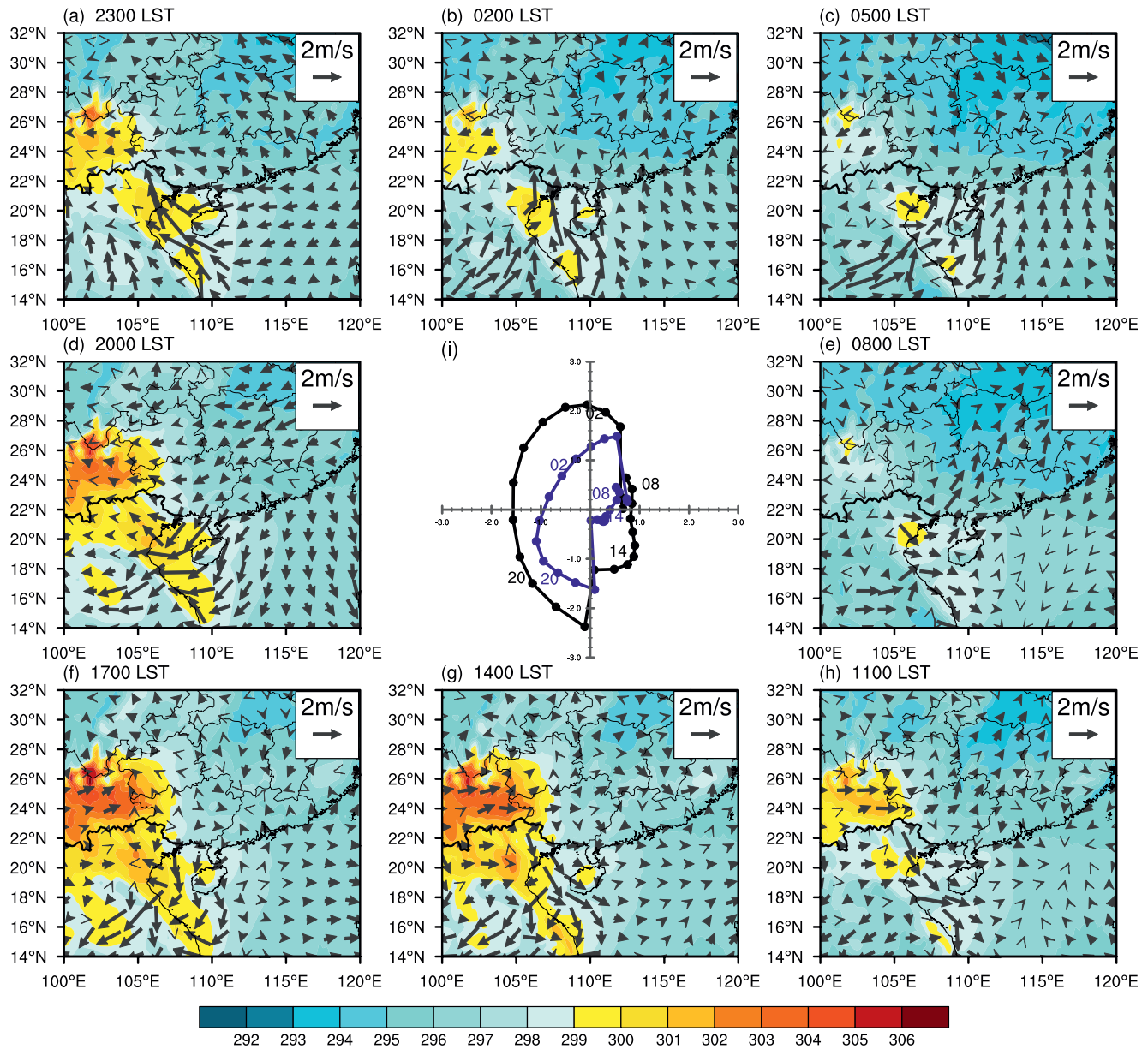


**Figure 7.** Diurnal variation of the 925 hPa wind deviations (vectors; units:  $\text{m s}^{-1}$ ) and air temperature (shading; units: K) on double boundary layer jet (BLJ) days from the ERA5 data set at (a) 2300, (b) 0200, (c) 0500, (d) 2000, (e) 0800, (f) 1700, (g) 1400, and (h) 1100 LST. (i) Hodograph of the wind deviations at 925 hPa over the Beibu Gulf (black line, averaged over BLJ-West box in Figure 6) and the coastal area of Guangdong (blue line, averaged over the BLJ-East box in Figure 6) on double BLJ days.

temperature and meridional winds in both the REMO and ROM showed a similar vertical structure to that in the ERA5 (Figures 9a–9c). In detail, the ROM clearly corrected the overestimated air temperature in the 950–800 hPa layer (Figures 9d–9f). The largest temperature differences between the ROM and REMO were in the boundary layer (Figure 9f). Similar results were also seen in the vertical cross-section of the Guangdong coast, where the ROM also reduces the air temperature bias over the sea and in the lower troposphere (Figures 9g–9i).

We examined the diurnal variation of the air temperature deviations, defined as the difference between the hourly and the daily mean air temperature, and the meridional wind deviations, in the two vertical cross-sections to explore why the large-scale land–sea thermal contrast was lower in the ROM. Once again, we used the meridional wind deviations in the ERA5 data set as the reference condition. This wind deviations clearly showed two strong ageostrophic flows at about 1700 and 0600 LST and a clear inertial oscillation at night between 2000 and 0500

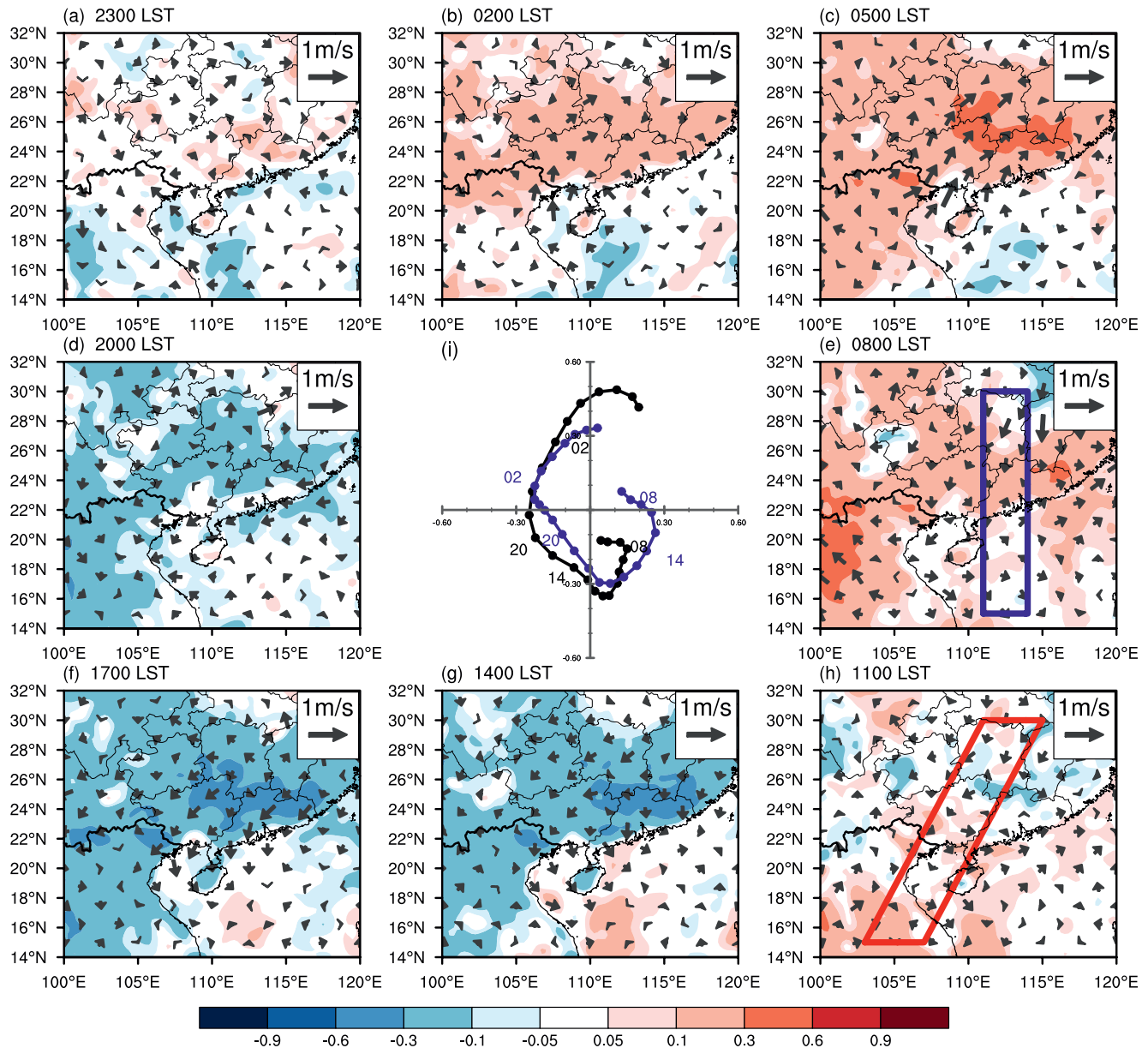


**Figure 8.** Diurnal variation of the wind deviations (vectors; units:  $\text{m s}^{-1}$ ) and air temperature (shading; units: K) at 925 hPa on double boundary layer jet (BLJ) days from the ROM-REMO at (a) 2300, (b) 0200, (c) 0500, (d) 2000, (e) 0800, (f) 1700, (g) 1400, and (h) 1100 LST. (i) Hodograph of the wind deviations at 925 hPa over the Beibu Gulf (black line, averaged over BLJ-West box in Figure 6) and the coastal area of Guangdong (blue line, averaged over the BLJ-East box in Figure 6) on double BLJ days.

LST (Figure 10i). The ROM and REMO showed a similar diurnal variance of the air temperature deviations and the meridional wind deviations. At night, the temperature decreased over land more slowly in the ROM than in the REMO (Figures 11a–11c). In addition, during the day the temperature increased over land more slowly during the day in the ROM than in the REMO (Figures 11f–11h), which indicates that the land–sea thermal contrast was smaller in the ROM than in the REMO, both during the afternoon and at night. A similar process was seen in the BLJ-East vertical cross-section, where there was also a slower changing boundary temperature over land in the ROM.

The stronger SST standard deviation appears in the ROM in the central SCS (Figure 3j), which means the atmosphere transmits energy to the ocean, which cools the boundary layer over land and heats the ocean during the day, leading to a warmer air temperature over the central SCS (Figure 8e–8h). However, the ocean transmits energy to the atmosphere and heats the boundary layer over land at night and therefore the SST and the air temperature over



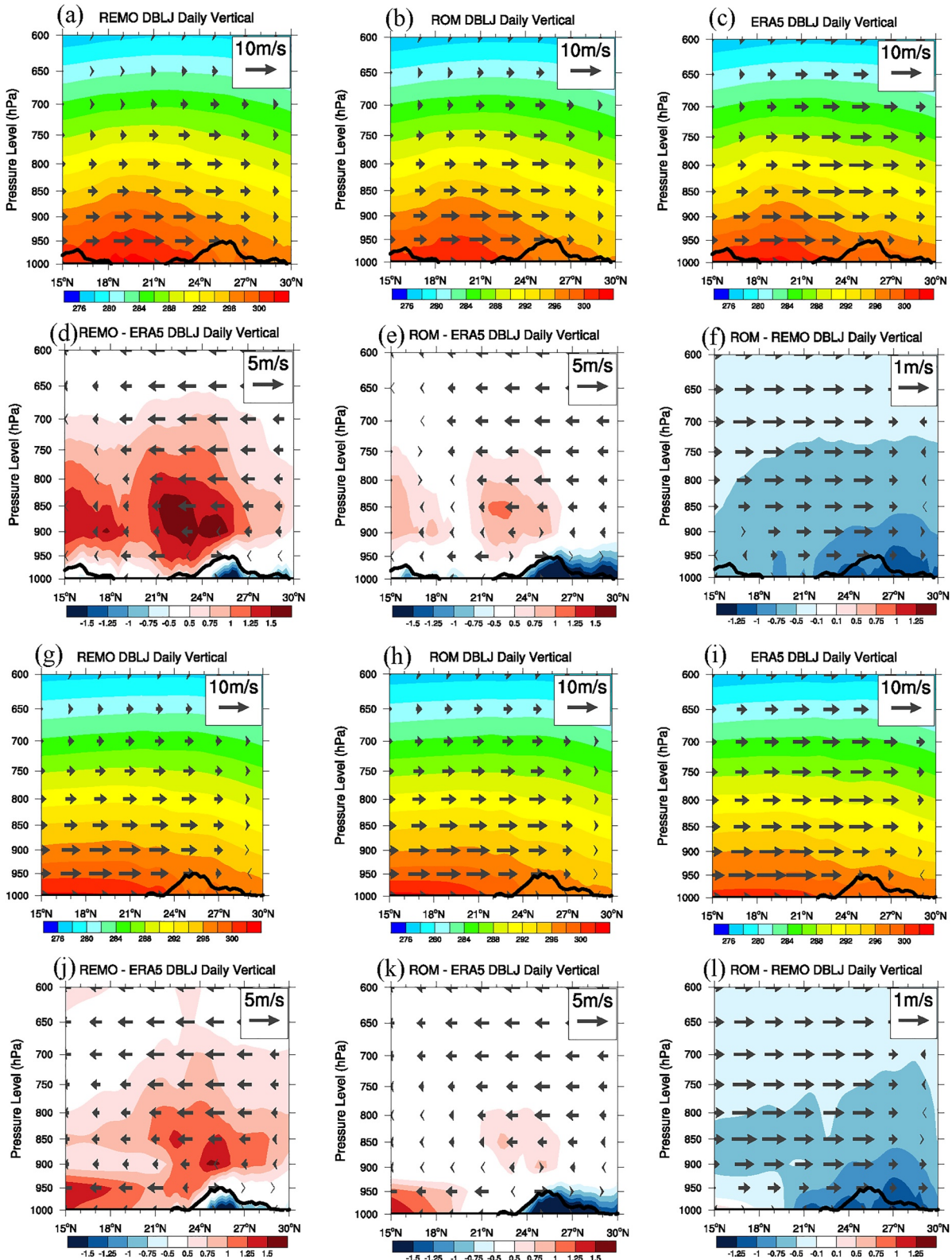


**Figure 9.** Composite vertical cross-sections of the air temperature (shading; units: K) and meridional winds (vectors; units:  $\text{m s}^{-1}$ ) averaged in the red box in Figure 8h from the (a) REMO, (b) ROM, (c) ERA5 data set, (d) bias REMO-ERA5, (e) bias ROM-ERA5, (f) the difference (ROM – REMO), averaged in the blue box in Figure 8c from the (g) REMO, (h) ROM, (i) ERA5 data set, (j) bias REMO-ERA5, (k) bias ROM-ERA5, and (l) the difference (ROM – REMO). The solid black line indicates the topography.



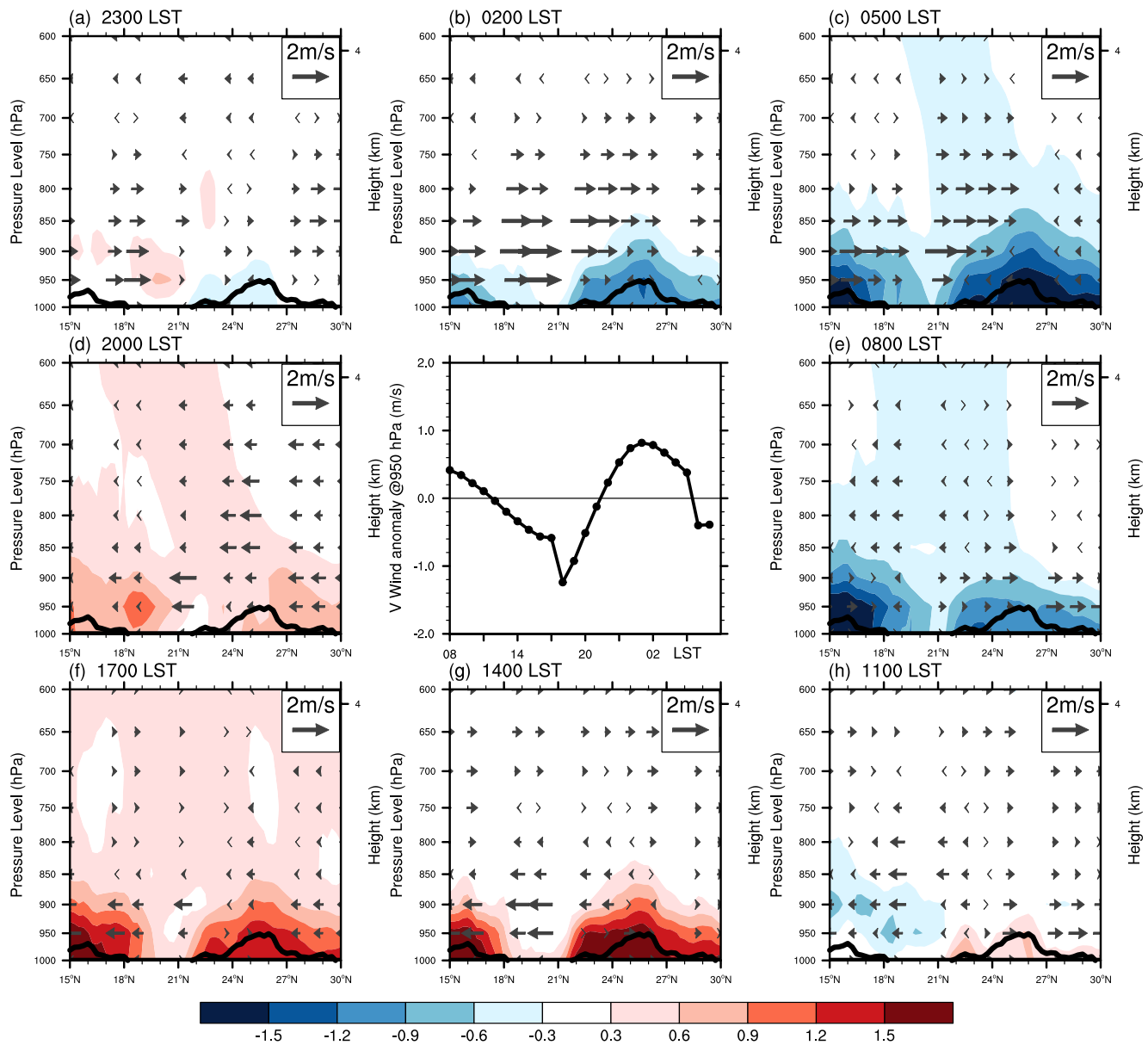


**Figure 10.** Composite vertical cross-sections of the diurnal variation of the air temperature deviations (shading; units: K) and the meridional wind deviations (vectors; units:  $\text{m s}^{-1}$ ) in the red box in Figure 8h on double boundary layer jet days for the ERA5 reanalysis data set at (a) 2300, (b) 0200, (c) 0500, (d) 2000, (e) 0800, (f) 1700, (g) 1400, and (h) 1100 hr LST. (i) Hodograph of the meridional winds at 950 hPa averaged in the red box in Figure 8h. The black solid line indicates the topography.

the central SCS decreases (Figures 8a–8c). These processes increase the standard deviation of the SST over the central SCS and weaken the large-scale land–sea thermal contrast in the ROM (e.g., in the 925 hPa layer). This leads to a more obvious inertial oscillation, which causes the ageostrophic flows to veer (Figure 8i). The inertial oscillation is important in BLJ events and can cause the northeasterly ageostrophic flow over the Beibu Gulf in the afternoon and the easterly ageostrophic flow off the coastline of Guangdong at night to veer to the southwest, the direction of the maximum wind speed on BLJ days, leading to a stronger southwesterly wind on BLJ days in the ROM than in the REMO.

#### 4. Summary and Discussion

Operational numerical weather prediction is currently carried out using standalone atmospheric models and prescribed SSTs. The prescribed SST can improve the ability of models to simulate the BLJ (Gao et al., 2022), but not in coastal areas. The BLJ is a key factor in the diurnal cycle of heavy rain (Du et al., 2022), especially over

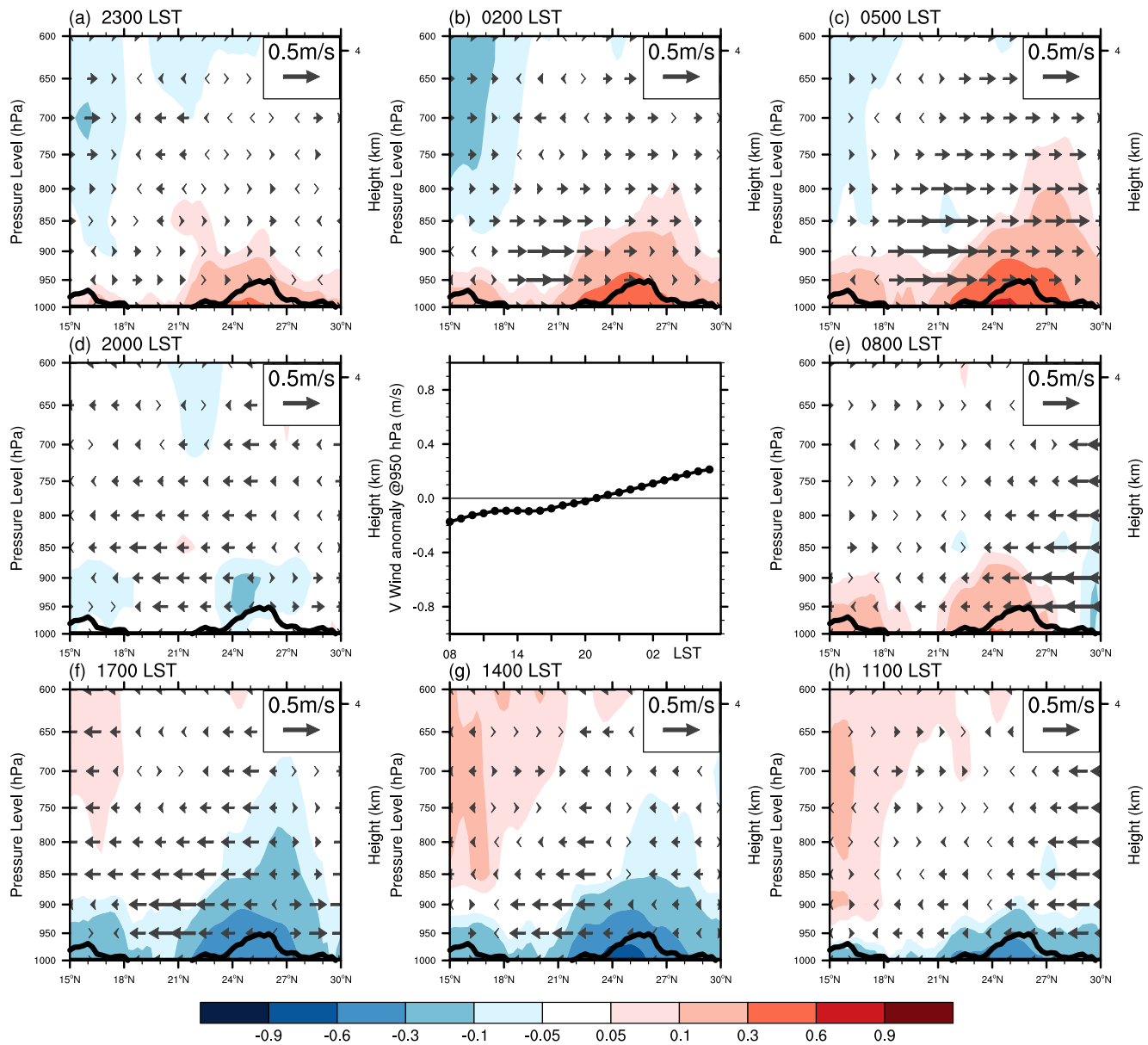


**Figure 11.** Composite vertical cross-sections of the diurnal variation of the air temperature deviations (shading; units: K) and the meridional wind deviations (vectors; units:  $\text{m s}^{-1}$ ) in the red box in Figure 8h on double boundary layer jet days for the ROM-REMO at (a) 2300, (b) 0200, (c) 0500, (d) 2000, (e) 0800, (f) 1700, (g) 1400, and (h) 1100 hr LST. (i) Hodograph of the meridional winds at 950 hPa averaged in the red box in Figure 8h. The black solid line indicates the topography.

coastal areas, because it supplies both moisture and dynamic lifting. We analyzed 33-year simulations with an atmosphere–ocean coupled model, the ROM, and its uncoupled component, the REMO, forced by the prescribed SST. We validated these models with the TRMM TMI SST and the ERA5 hourly reanalysis data set and found that the coupled model ROM gave a more realistic SST than the REMO on BLJ days. The ROM corrected the overestimated daytime air temperature over land in the REMO on BLJ days. The ROM showed a lower land–sea thermal contrast in the boundary layer. This increased the inertial oscillation effects, which can cause the north-easterly ageostrophic flow over the Beibu Gulf in the afternoon and the easterly ageostrophic flow off the coast of Guangdong at night to veer to the southwest, which is the direction of the maximum wind speed on BLJ days. The ROM reproduced a more reasonable land–sea thermal contrast in the boundary layer as a result of strong air–sea mixing over the coast, which gave rise to a larger inertial oscillation and a standard deviation of the SST over the central SCS. These findings deepen our understanding of the influence of a fully mixed air–sea boundary on coastal weather processes. Our results can be summarized as follows.

1. There are two high-frequency regions for BLJs: one located over the Beibu Gulf (BLJ-West) and the other over the coastal area of Guangdong (BLJ-East). Double BLJ days constitute the majority of BLJ-West and BLJ-East days. The REMO and ROM can both represent the actual distribution and variance of the monthly mean SST on BLJ days. The magnitude of the standard deviation of the SST in the ROM is significantly greater than that in the REMO and is more realistic, indicating the importance of the ocean response to air–sea mixing processes in the ROM.
2. The ROM simulates a much higher probability of wind speeds  $>9 \text{ m s}^{-1}$  than the REMO. The probability distribution of all the wind speeds in the BLJ-West area and the wind speeds of about  $10 \text{ m s}^{-1}$  in the BLJ-East area in the ROM agree well with those from the ERA5 data set. Based on the daily mean wind field and the distribution of the surface air temperature, the ROM corrects the overestimated air temperature over the land on both BLJ-West and BLJ-East days and gives a more realistic land–sea thermal contrast than the REMO.
3. The effects of the large-scale land–sea thermal contrast and inertial oscillation on the wind deviations have a see-saw relationship. The inertial oscillation is more robust in the ROM than in the REMO, as shown by a clear clockwise rotation in the differences in the diurnal variance of the wind deviations between the ROM and the REMO. The inertial oscillation is one of the triggers of BLJ events and can cause the northeasterly ageostrophic flow over the Beibu Gulf in the afternoon and the easterly ageostrophic flow off the coastline of Guangdong to veer southwest at night, which is the direction of the maximum wind speed on BLJ days.
4. In the coupled model, the ocean receives energy from the atmosphere during the day and release energy back to the atmosphere at night as a result of the fully mixed air–sea boundary in coastal weather processes. This decreases the variability of the air temperature in the boundary layer and the large-scale land–sea thermal contrast, which gives rise to a more obvious inertial oscillation and a greater standard deviation of the SST over the central SCS in the ROM than in the REMO.

To sustain a clear focus in this study, we limited our discussion to the main mechanism of the atmosphere–ocean coupled model that enhances the predictability of BLJ events through influencing the large-scale land–sea thermal contrast and inertial oscillation in the boundary layer. However, other factors such as hydraulic jumps and orography can also impact coastal BLJs. Future work will investigate the relationship between coastal BLJs and precipitation.

#### Acknowledgments

This work was jointly supported by the National Natural Science Foundation of China (Grant 42275164) entitled “Research on 8–42d Subseasonal Multi-mode Integrated Forecasting Based on Statistical Methods and Machine Learning,” National Key Research and Development Project of China (Grant 2017YFC1502002), and “the Priority Academic Program Development of Jiangsu Higher Education Institutions” (PAPD). Dmitry Sein worked in the framework of the SIO RAS state assignment (No FMWE-2021-0014) and was also supported by the Federal Ministry of Education and Research of Germany (BMBF) in the framework of ACE project (Grant 01LP2004A). William Cabos has been funded by the Alcala University project PIUAH21/CC-058 and the Spanish Ministry of Science, Innovation and Universities, through Grant (PID2021-128656OB-I00). We thank to the ECMWF for providing ERA5 data, Asia-Pacific Data-Research Center for supplying TRMM TMI SST data and China Meteorological Administration for the best-track TCs data. We thank the Climate System Department at GERICs for the consultations on the REMO model. Simulations were done at the German Climate Computing Center (DKRZ). The authors also acknowledge the High Performance Computing Center of Nanjing University of Information Science and Technology for their support of this work. Open Access funding enabled and organized by Projekt DEAL.

#### Conflict of Interest

The authors declare no conflicts of interest relevant to this study.

#### Data Availability Statement

The data used in the paper are available at <https://doi.org/10.5281/zenodo.8175038>. TRMM TMI SST data are supplied by Asia-Pacific Data-Research Center at <http://apdrc.soest.hawaii.edu/data/> and the best-track TCs data are provided by the China Meteorological Administration at [https://tcdata.typhoon.org.cn/en/zjljsjj\\_zlhc.html](https://tcdata.typhoon.org.cn/en/zjljsjj_zlhc.html) and described by Lu et al. (2021). The reanalysis data set ERA5 reanalysis are offered by the Copernicus Climate Change Service (C3S, 2017): <https://cds.climate.copernicus.eu/#/home>.

#### References

- Arakawa, A., & Lamb, V. R. (1977). Computational design of the basic dynamical processes of the UCLA general circulation model. *Methods in Computational Physics*, 17, 173–265.
- Asselin, R. (1972). Frequency filter for time integrations. *Monthly Weather Review*, 100(6), 487–490. [https://doi.org/10.1175/1520-0493\(1972\)100<0487:fffti>2.3.co;2](https://doi.org/10.1175/1520-0493(1972)100<0487:fffti>2.3.co;2)
- Blackadar, A. K. (1957). Boundary layer wind maxima and their significance for the growth of nocturnal inversions. *Bulletin of the American Meteorological Society*, 38(5), 283–290. <https://doi.org/10.1175/1520-0477-38.5.283>
- Browne, P. A., de Rosnay, P., Zuo, H., Bennett, A., & Dawson, A. (2019). Weakly coupled ocean–atmosphere data assimilation in the ECMWF NWP system. *Remote Sensing*, 11(3), 234. <https://doi.org/10.3390/rs11030234>
- Chen, D., Liu, W. T., Tang, W., & Wang, Z. (2003). Air–sea interaction at an oceanic front: Implications for frontogenesis and primary production. *Geophysical Research Letters*, 30(14), 1745. <https://doi.org/10.1029/2003GL017536>
- Chen, G., Lan, R., Zeng, W., Pan, H., & Li, W. (2018). Diurnal variations of rainfall in surface and satellite observations at the monsoon coast (South China). *Journal of Climate*, 31(5), 1703–1724. <https://doi.org/10.1175/jcli-d-17-0373.1>
- Copernicus Climate Change Service (C3S). (2017). ERA5: Fifth generation of ECMWF atmospheric reanalyses of the global climate [Dataset]. Copernicus Climate Change Service Climate Data Store (CDS). Retrieved from <https://cds.climate.copernicus.eu/#/home>
- Dai, A., & Deser, C. (1999). Diurnal and semidiurnal variations in global surface wind and divergence fields. *Journal of Geophysical Research*, 104(D24), 31109–31125. <https://doi.org/10.1029/1999JD900927>

- Dai, A., & Wang, J. (1999). Diurnal and semidiurnal tides in global surface pressure fields. *Journal of the Atmospheric Sciences*, 56(22), 3874–3891. [https://doi.org/10.1175/1520-0469\(1999\)056<3874:DASTIG>2.0.CO;2](https://doi.org/10.1175/1520-0469(1999)056<3874:DASTIG>2.0.CO;2)
- Dong, F., Zhi, X., Zhang, L., & Ye, C. (2021). Diurnal variations of coastal boundary layer jets over the Northern South China Sea and their impacts on diurnal cycle of rainfall over southern China during the early-summer rainy season. *Monthly Weather Review*, 149(10), 3341–3363. <https://doi.org/10.1175/mwr-d-20-0292.1>
- Du, Y., & Chen, G. (2019). Climatology of low-level jets and their impact on rainfall over southern China during the early-summer rainy season. *Journal of Climate*, 32(24), 8813–8833. <https://doi.org/10.1175/jcli-d-19-0306.1>
- Du, Y., Chen, Y.-L., & Zhang, Q. (2015). Numerical simulations of the boundary layer jet off the southeastern coast of China. *Monthly Weather Review*, 143(4), 1212–1231. <https://doi.org/10.1175/mwr-d-14-00348.1>
- Du, Y., & Rotunno, R. (2014). A simple analytical model of the nocturnal low-level jet over the great plains of the United States. *Journal of the Atmospheric Sciences*, 71(10), 3674–3683. <https://doi.org/10.1175/jas-d-14-0060.1>
- Du, Y., Shen, Y., & Chen, G. (2022). Influence of coastal marine boundary layer jets on rainfall in South China. *Advances in Atmospheric Sciences*, 39(5), 782–801. <https://doi.org/10.1007/s00376-021-1195-7>
- Gao, X., Luo, Y., Lin, Y., & Bao, X. (2022). A source of WRF simulation error for the early-summer warm-sector heavy rainfall over south China coast: Land-sea thermal contrast in the boundary layer. *Journal of Geophysical Research: Atmospheres*, 127(4), e2021JD035179. <https://doi.org/10.1029/2021jd035179>
- Gentemann, C. L., Wentz, F. J., Mears, C. A., & Smith, D. K. (2004). In situ validation of tropical rainfall measuring mission microwave sea surface temperatures. *Journal of Geophysical Research*, 109(C4), C04021. <https://doi.org/10.1029/2003JC002092>
- Hagemann, S., & Dümenil (1997). A parametrization of the lateral waterflow for the global scale. *Climate Dynamics*, 14(1), 17–31. <https://doi.org/10.1007/s003820050205>
- Hagemann, S., & Dümenil, L. (1998). A parameterization of the lateral waterflow for the global scale. *Climate Dynamics*, 14(1), 17–31. <https://doi.org/10.1007/s003820050205>
- Hagemann, S., & Gates, L. D. (2001). Validation of the hydrological cycle of ECMWF and NCEP reanalyses using the MPI hydrological discharge model. *Journal of Geophysical Research*, 106(D2), 1503–1510. <https://doi.org/10.1029/2000jd900568>
- Hersbach, H., Bell, B., Berrisford, P., Hirahara, S., Horányi, A., Muñoz-Sabater, J., et al. (2020). The ERA5 global reanalysis. *Quarterly Journal of the Royal Meteorological Society*, 146(730), 1999–2049. <https://doi.org/10.1002/qj.3803>
- Huang, W. R., Chan, J. C. L., & Wang, S.-Y. (2010). A planetary-scale land–sea breeze circulation in East Asia and the western North Pacific. *Quarterly Journal of the Royal Meteorological Society*, 136(651), 136–1553. <https://doi.org/10.1002/qj.663>
- Jacob, D. (2001). A note to the simulation of the annual and inter-annual variability of the water budget over the Baltic Sea drainage basin. *Meteorology and Atmospheric Physics*, 77(1–4), 61–73. <https://doi.org/10.1007/s007030170017>
- Jacob, D., Hurk, B. J. J. M. V. D., Andræ, U., Elgered, G., Fortelius, C., Graham, L. P., et al. (2001). A comprehensive model inter-comparison study investigating the water budget during the BALTEX-PIDCAP period. *Meteorology and Atmospheric Physics*, 77(1), 19–43. <https://doi.org/10.1007/s007030170015>
- Jungclaus, J. H., Fischer, N., Haak, H., Lohmann, K., Marotzke, J., Matei, D., et al. (2013). Characteristics of the ocean simulations in the max Planck institute ocean model (MPIOM) the ocean component of the MPI-Earth system model. *Journal of Advances in Modeling Earth Systems*, 5(2), 422–446. <https://doi.org/10.1002/jame.20023>
- Kalverla, P. C., Duncan, J. B., Jr., Steeneveld, G. J., & Holtslag, A. A. M. (2019). Low-level jets over the North Sea based on ERA5 and observations: Together they do better. *Wind Energy Science*, 4(2), 193–209. <https://doi.org/10.5194/wes-4-193-2019>
- Kong, H., Zhang, Q., Du, Y., & Zhang, F. (2020). Characteristics of coastal low-level jets over Beibu Gulf, China, during the early warm season. *Journal of Geophysical Research: Atmospheres*, 125(14), e2019JD031918. <https://doi.org/10.1029/2019JD031918>
- Lu, X., Yu, H., Ying, M., Zhao, B., Zhang, S., Lin, L., et al. (2021). Western North Pacific tropical cyclone database created by the China meteorological administration. *Advances in Atmospheric Sciences*, 38(4), 690–699. <https://doi.org/10.1007/s00376-020-0211-7>
- Luo, Y., Wu, M., Ren, F., Li, J., & Wong, W.-K. (2016). Synoptic situations of extreme hourly precipitation over China. *Journal of Climate*, 29(24), 8703–8719. <https://doi.org/10.1175/JCLI-D-16-0057.1>
- Majewski, D. (1991). The Europa-Modell of the Deutscher Wetterdienst. In *Paper presented at ECMWF Seminar on numerical methods in atmospheric models*.
- Marsland, S. J., Haak, H., Jungclaus, J. H., Latif, M., & Röske, F. (2003). The Max-Planck-Institute global ocean/sea ice model with orthogonal curvilinear coordinates. *Ocean Modelling*, 5(2), 91–127. [https://doi.org/10.1016/s1463-5003\(02\)00015-x](https://doi.org/10.1016/s1463-5003(02)00015-x)
- Ren, F., Wang, Y., Wang, X., & Li, W. (2007). Estimating tropical cyclone precipitation from station observations. *Advances in Atmospheric Sciences*, 24(4), 700–711. <https://doi.org/10.1007/s00376-007-0700-y>
- Ren, F., Wu, G., Dong, W., Wang, X., Wang, Y., Ai, W., & Li, W. (2006). Changes in tropical cyclone precipitation over China. *Geophysical Research Letters*, 33(20), L20702. <https://doi.org/10.1029/2006GL027951>
- Roeckner, E., Arpe, K., Bentsson, L., Christoph, M., Claussen, M., Umenil, L. D., et al. (1996). The atmospheric general circulation model ECHAM-4: Model description and simulation of present-day climate. *Comptes Rendus des Seances de la Societe de Biologie et de Ses Filiales*, 151(2), 361–363.
- Roeckner, E., Bäuml, G., Bonaventura, L., Brokopf, R., Esch, M., Giorgetta, M., et al. (2003). The atmospheric general circulation model ECHAM 5. PART I: Model description.
- Sein, D. V., Koldunov, N. V., Danilov, S., Wang, Q., Sidorenko, D., Fast, I., et al. (2017). Ocean modeling on a mesh with resolution following the local Rossby radius. *Journal of Advances in Modeling Earth Systems*, 9(7), 2601–2614. <https://doi.org/10.1002/2017ms001099>
- Sein, D. V., Mikolajewicz, U., Gröger, M., Fast, I., Cabos, W., Pinto, J. G., et al. (2015). Regionally coupled atmosphere-ocean-sea ice-marine biogeochemistry model ROM: I. Description and validation. *Journal of Advances in Modeling Earth Systems*, 7(1), 268–304. <https://doi.org/10.1002/2014ms000357>
- Simmons, A. J., & Burridge, D. M. (1981). An energy and angular-momentum conserving vertical finite-difference scheme and hybrid vertical coordinates. *Monthly Weather Review*, 109(4), 758–766. [https://doi.org/10.1175/1520-0493\(1981\)109<0758:aeaamc>2.0.co;2](https://doi.org/10.1175/1520-0493(1981)109<0758:aeaamc>2.0.co;2)
- Sinclair, M. R. (2004). Extratropical transition of southwest Pacific tropical cyclones. Part II: Midlatitude circulation characteristics. *Monthly Weather Review*, 132(9), 2145–2168. [https://doi.org/10.1175/1520-0493\(2004\)132<2145:Etoept>2.0.Co;2](https://doi.org/10.1175/1520-0493(2004)132<2145:Etoept>2.0.Co;2)
- Tu, C.-C., Chen, Y.-L., Lin, P.-L., & Du, Y. (2019). Characteristics of the marine boundary layer jet over the South China Sea during the early summer rainy season of Taiwan. *Monthly Weather Review*, 147(2), 457–475. <https://doi.org/10.1175/mwr-d-18-0230.1>
- Valcke, C. A., Declat, D., & Terray, L. (2010). OASIS3 ocean atmosphere sea ice soil user's guide.
- Valcke, S., Craig, T., & Coquart, L. (2015). OASIS3-MCT user guide OASIS3-MCT 3.0Rep., technical report. TR/CMGC/15/38, CERFACS/CNRS SUC URA.

- Wentz, G., Gentemann, C., Smith, D., & Chelton, D. (2000). Satellite measurements of sea surface temperature through clouds. *Science*, 288(5467), 847–850. <https://doi.org/10.1126/science.288.5467.847>
- Wu, N., Ding, X., Wen, Z., Chen, G., Meng, Z., Lin, L., & Min, J. (2020). Contrasting frontal and warm-sector heavy rainfalls over South China during the early-summer rainy season. *Atmospheric Research*, 2020(235), 104693. <https://doi.org/10.1016/j.atmosres.2019.104693>
- Wu, R. (2010). Subseasonal variability during the South China Sea summer monsoon onset. *Climate Dynamics*, 34(5), 629–642. <https://doi.org/10.1007/s00382-009-0679-4>
- Xu, J., Koldunov, N., Remedio, A. R. C., Sein, D. V., Zhi, X., Jiang, X., et al. (2019). On the role of horizontal resolution over the Tibetan Plateau in the REMO regional climate model. *Climate Dynamics*, 51(11–12), 4525–4542. <https://doi.org/10.1007/s00382-018-4085-7>
- Zhang, M., & Meng, Z. (2019). Warm-sector heavy rainfall in southern China and its WRF simulation evaluation: A low-level-jet perspective. *Monthly Weather Review*, 147(12), 4461–4480. <https://doi.org/10.1175/mwr-d-19-0110.1>
- Zhu, S., Remedio, A. R. C., Sein, D. V., Sielmann, F., Ge, F., Xu, J., et al. (2020). Added value of the regionally coupled model ROM in the East Asian summer monsoon modeling. *Theoretical and Applied Climatology*, 140(1), 375–387. <https://doi.org/10.1007/s00704-020-03093-8>